Journal of Alloys and Compounds 871 (2021) 159557

Contents lists available at ScienceDirect

Journal of Alloys and Compounds

journal homepage: www.elsevier.com/locate/jalcom

In situ study on the compression deformation of MoNbTaVW high-entropy alloy

Congyan Zhang[a,1], Binbin Yue[b,1], Uttam Bhandari[a], Oleg N. Starovoytov[c], Yan Yang[a], David P. Young[d], Jinyuan Yan[e], Fang Hong[f,g,h,*], Shizhong Yang[a,**]

[a] Department of Computer Science, Southern University and A&M College, Baton Rouge, LA 70813, USA
[b] Center for High Pressure Science and Technology Advanced Research, Beijing 100094, China
[c] Department of Materials Chemistry, Nagoya University, Furo-cho, Chikusa-ku, Nagoya 464-8603, Japan
[d] Department of Physics & Astronomy, Louisiana State University, Baton Rouge, LA 70803, USA
[e] Lawrence Berkeley National Laboratory, Berkeley, CA 94720, USA
[f] Beijing National Laboratory for Condensed Matter Physics, Institute of Physics, Chinese Academy of Sciences, Beijing 100190, China
[g] School of Physical Sciences, University of Chinese Academy of Sciences, Beijing 100190, China
[h] Songshan Lake Materials Laboratory, Dongguan, Guangdong 523808, China

ARTICLE INFO

Article history:
Received 13 January 2021
Received in revised form 18 February 2021
Accepted 15 March 2021
Available online 17 March 2021

Keywords:
High-entropy alloy
Compression deformation
Synchrotron X-ray diffraction
Diamond anvil cell
Density functional theory
Texture

ABSTRACT

The excellent mechanical properties of high-entropy alloys (HEAs) make them promising materials for advances in science and technology. However, the underlying mechanism of plastic deformation is not well understood. *In situ* experiments are urgently required to provide a fundamental understanding of the plastic deformation under high pressure. We performed *in situ* synchrotron X-ray diffraction (XRD) experiments to study compression deformation behavior of the HEA MoNbTaVW in a radial diamond anvil cell (rDAC). Our results show that the strength and ratio of the stress-to-shear modulus values are ~1.5 and 3 times that of pure tungsten (W), respectively. MoNbTaVW showed plastic deformation above 5 GPa and displayed a much stronger texture. We found that the active dislocation behavior is mainly responsible for the high strength in MoNbTaVW under compression. This unique technique opens a new avenue to investigate the *in situ* mechanical properties and their mechanism in other types of HEAs.

1. Introduction

Compared with pure metals, high-entropy alloys (HEAs) have demonstrated many promising properties [1–4], such as high strength at both room temperature and high temperature [5], exceptional ductility and toughness [6], and they are considered as a new class of advanced structural materials. The studies on refractory HEAs were inspired by their wide range of fundamental properties, which provide the high flexibility of refractory HEAs. As one typical example of a refractory HEA, the body-centered cubic (BCC) MoNbTaVW has shown high hardness and exceptional strength at temperatures up to 1900 K [7,8]. Coarse-grained MoNbTaVW showed a high Vickers micro-hardness of 5250 MPa [9], while nanocrystalline MoNbTaVW, with an average particle size of ~30 nm, had a high hardness of 11.4 GPa at 1150 °C [8]. On the other hand, the yield stress of MoNbTaVW with grain size of ~80 μm was measeured using standard compression techniques (Instron mechanical testing machine). It is 1246 MPa at room temperature and only decreases to 842 MPa at 1000 °C [7]. The yield stress has been shown to be extremely sensitive to the length scale of the microstructure, which depends on synthesis conditions. Maresca and Curtin [10] presented a theory of edge-dislocation strengthening in BCC random alloys to rationalize the strength of MoNbTaVW and other BCC HEAs. Since the random field of solutes in these high-concentration alloys creates large energy barriers for thermally activated edge glide, the strength of BCC HEAs can be controlled by edge dislocations, especially at high temperatures.

In the past several years, many experimental efforts have also been made on understanding the mechanism responsible for the HEAs outstanding mechanical properties [11–13], which is crucial for material design and realistic application of high performance HEAs.

* Corresponding author at: Beijing National Laboratory for Condensed Matter Physics, Institute of Physics, Chinese Academy of Sciences, Beijing 100190, China.
** Corresponding author.
E-mail addresses: hongfang@iphy.ac.cn (F. Hong), shizhong_yang@subr.edu (S. Yang).
[1] Congyan Zhang and Binbin Yue contributed equally to this work.

https://doi.org/10.1016/j.jallcom.2021.159557
0925-8388/

Traditional mechanical testing, whether tensile or compressive experiments, typically utilize *ex situ* methods to characterize the microstructure. Common examples include, the investigation of grain size and deformation texture by scanning electron microscopy (SEM) and electron backscatter diffraction (EBSD) [14], element distribution by energy dispersive spectroscopy (EDS) [15], and plastic deformation and defect (such as twinning, dislocation) behavior by transmission electron microscopy (TEM) [4,16,17]. Compression techniques have also been used to investigate deformation mechanical behavior and its mechanism by studying the samples *ex situ* after compression [18]. There are some tentative works that incorporate TEM with tension stage, which allows one to monitor the dislocation formation and movement *in situ* [15]. Nevertheless, *in situ* investigations, as a function of temperature and pressure, are still urgently required, if the active deformation mechanisms in HEAs are to be fully understood.

A diamond anvil cell (DAC) [19], which can easily generate high pressure by compressing small samples between two opposing diamond culets, is widely used in material science to explore significant changes in the properties of materials induced by high pressure. Previously, DAC-based high-pressure techniques, especially high-pressure X-ray diffraction (XRD), have been used to investigate the phase transition of several 3D transition metal HEAs, such as CoCrFeMnNi, AlCoCrFeNi, and CoCrCuFeNi at the micrometer scale [20–25]. Compared with conventional axial XRD, the technique of radial XRD in a radial DAC (rDAC) makes it possible to investigate the texture and lattice strain in stressed crystals *in situ*. For example, *in situ* observation of plastic deformation and active grain rotation in nanometer-scaled Ni were reported by applying the rDAC XRD technique [26,27]. A similar technique was also used to reveal the martensitic transition mechanism in oxides under high pressure [28,29]. For superhard materials, the rDAC technique has become a powerful *in situ* tool to study their elastic and plastic mechanical properties, such as bulk modulus, shear stress, and yield stress [30,31]. Most importantly, the data collected from the rDAC XRD method have a much better statistical reliability because of the large sample volume (μm^3 scale), compared with a local study done by TEM (nm^3 scale). Therefore, the rDAC XRD technique is a powerful *in situ* characterization method to study the deformation behavior of materials, including HEAs.

In this work, the rDAC XRD experiments were carried out *in situ* to study the deformation behavior of the HEA MoNbTaVW. The same study on pure W was also performed as a reference to illustrate the advanced properties of HEAs. The first principles density functional theory (DFT) based simulations were employed as an accessorial tool to help understand the mechanism of the mechanical properties under high pressure. Our study shows that MoNbTaVW displayed much higher strength and stronger texture than those of pure W. This work clearly demonstrated that the active dislocation behavior is mainly responsible for the high-strength properties observed in MoNbTaVW under compression. The unique technique used in this work can be applied to study the mechanical properties and their mechanism in other types of HEAs.

2. Experiments and computational methods

The MoNbTaVW sample was prepared by arc melting on a water-cooled copper hearth under an argon atmosphere. The powders used in synthesizing the alloy with purity higher than 99.9% were mixed with equal atomic ratios and pressed to a cylindrical shape. After melting, the compounds were inverted and re-melted several times to ensure chemical homogeneity. The MoNbTaVW sample was then cut into small pieces and milled under normal temperature and pressure in the air to powder for the *in situ* high-pressure synchrotron XRD experiment. The average size of samples particles was 0.05–0.1 μm checked by SEM. The rDAC technique was employed to demonstrate the deformation behavior and texturing of stressed MoNbTaVW/Au and W/Au mixtures, in which Au was used as the pressure calibrant. As shown in Fig. 1(a), a Kapton supported boron gasket, which is X-ray transparent, was clamped by the opposing diamond culets. The samples were loaded into the center hole of the boron gasket, where the diameter of the gasket hole was 60 μm. The pressure was generated by evenly applying force to the opposing diamonds. *In situ* rDAC XRD data were collected at beamline 12.2.2 at the Advanced Light Source (ALS), Lawrence Berkeley National Laboratory (LBNL) with the X-ray wavelength of 0.4133 Å. CeO_2 was used as the standard material to calibrate the sample-detector distance and orientation. The diffraction images were initially analyzed by Dioptas [32] to determine the pressure by fitting to the standard Au diffraction peaks. The measured 2D diffraction of both samples under ambient conditions, high pressure (~20 GPa), and back to ~1 GPa are shown in Fig. 1(b) and (c), in which the complete 110, 200, 211, 220, and 310 diffraction rings of MoNbTaVW and W are marked by the red arrows. The samples were uniaxially compressed in a rDAC, which produces large shear stress and triggers the generation of dislocations. Diffraction images were unrolled by integrating over 5° increments of azimuthal arcs, resulting in 72 spectra for each image. Then they were quantitatively analyzed for hydrostatic cell parameters, textures, stress, grain sizes and microstrains (heterogeneous strains) using Rietveld refinement [33] as implemented in the software package MAUD [34].

The first principles calculation of structural and mechanical properties in this work were carried out using the DFT [35,36] based Vienna Ab-initio Simulation Package (VASP 5.4) [37] installed in MedeA software. The electron-ion interactions were described by the projector augmented wave (PAW) [38] method, while electron exchange-correlation interactions were described by the generalized gradient approximation (GGA) [39] in the scheme of Perdew–Burke–Ernzerhof (PBE) [40]. A 5 × 5 × 5 supercell with 125-atom was built based on the primitive BCC unit cell (lattice vectors are a(1/2, 1/2, −1/2); a(1/2, −1/2, 1/2) and a(−1/2, 1/2, 1/2)). Based on this supercell, a special quasi-random structure (SQS) for five element alloys reported in Ref. [41] was selected for computational simulations, in which the supercell model has shown its reliability on predicting the properties of HEAs [41,42]. The structural relaxation was performed using the conjugate-gradient algorithm [43] implemented in VASP. An energy cutoff was set to be 500 eV for the plane wave basis sets in all calculations, and the criteria for the convergences of energy and force in relaxation processes were set to be 10^{-4} eV and 10^{-3} eV/nm, respectively. A 3 × 3 × 3 K-point mesh, *via* the Monkhorst–Pack method, was generated for performing Brillouin zone calculations.

3. Results and discussion

In situ XRD patterns of the MoNbTaVW/Au and W/Au mixtures during compression and decompression are shown in Fig. 2(a) and (b), respectively. The corresponding pressures which were determined by the standard Au XRD peaks are listed on the right side of each figure. As shown in the figures, all major peaks obtained under various pressure were characterized as FCC (the standard Au diffraction peaks) and BCC (MoNbTaVW). Furthermore, the lattice constant of MoNbTaVW at ambient conditions (black XRD pattern at the bottom of Fig. 2(a)) is 0.3195 nm (DFT calculation: 0.3194 nm), while the lattice constant of pure W is 0.3164 nm (DFT: 0.3164 nm). Since neither peak appear nor disappears, there was no phase transition obtained during compression with the pressure up to 20 GPa. It is also clearly shown that all diffraction peaks shift to larger 2θ angles with pressure and shift to smaller 2θ angles when the pressure is decreased. The corresponding 2θ angles for the 110, 200, 211 and 220 peaks as a function of pressure are shown in Fig. 2(c). The location of the diffraction peaks of MoNbTaVW show a

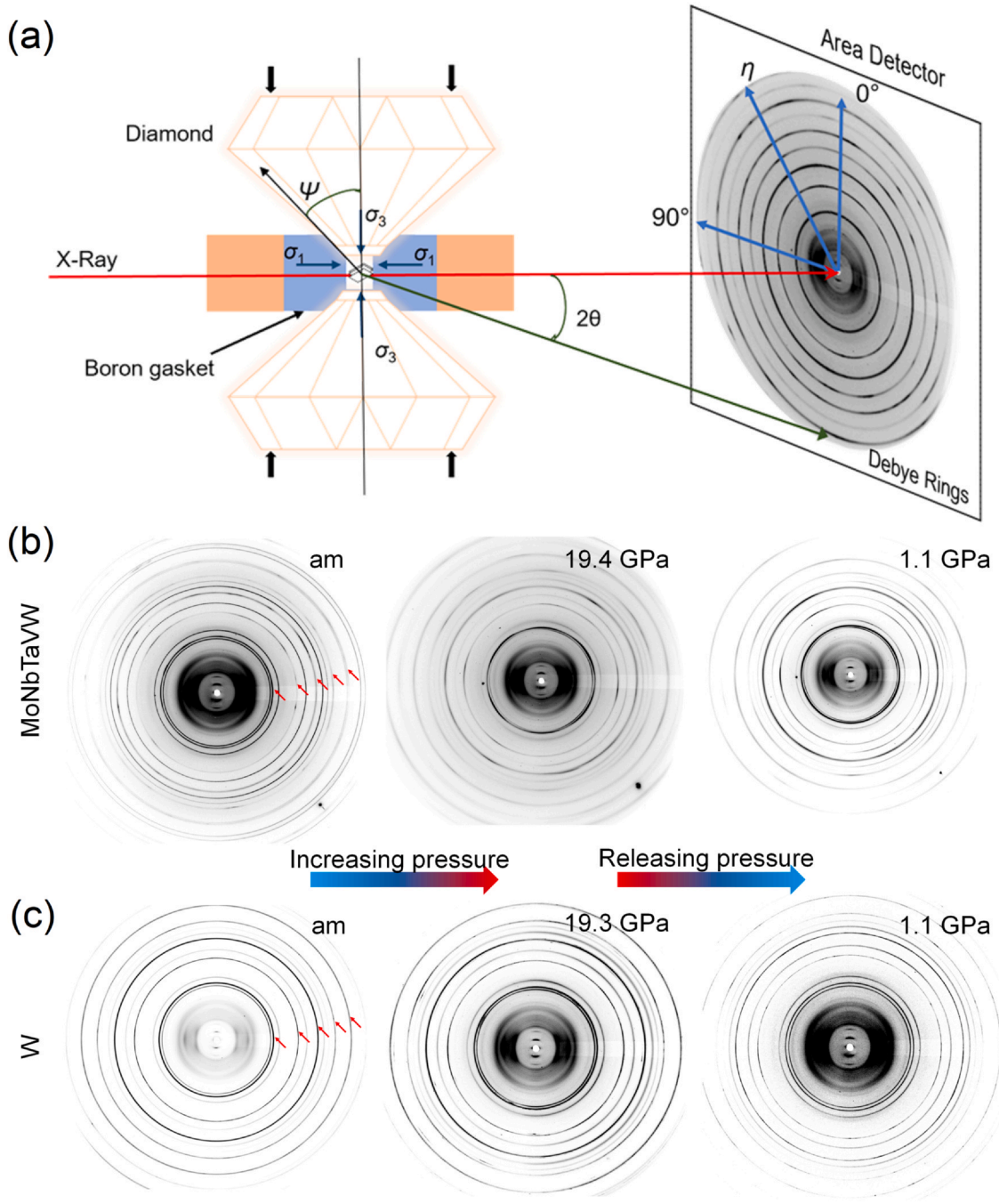

Fig. 1. (a) The illustration of the radial X-ray diffraction experiment in a diamond anvil cell (DAC). Representative radial diffraction images of (b) MoNbTaVW and (c) W under ambient condition, high pressure, and back to ~ 1 GPa. The BCC diffraction rings at ambient pressure are marked by the red arrows in the left panel of the figure.

greater angular dependance on applied pressure, which indicates MoNbTaVW shows a greater change in lattice constant. Moreover, due to the existence of multiple elements in the alloy, different intrinsic physical properties of these elements (for example, atom size, electronegativity, covalence electrons, and so on) may induce more local stress and defects in the BCC MoNbTaVW crystal, which lead to broader peaks than those of W. Consequently, the full width at half maximum (FWHM) of the MoNbTaVW diffraction peaks are also broader than those of pure W.

Based on the XRD patterns under various pressures, the volume per atom as a function of pressure for MoNbTaVW (red dots) and W (black dots) are demonstrated in Fig. 3(a). The corresponding lattice constants under various pressure are shown in Fig. 3(b) by the solid squares/circles. The inset of Fig. 3(b) shows a typical 125-atom SQS model. No obvious volume collapse was obtained under high pressure, indicating a stable phase of MoNbTaVW and W up to ~20 GPa. The volume–pressure curves in Fig. 3(a) were fitted by the third order Birch–Murnaghan isothermal equation of state (BM3-EOS) [44,45],

$$P = 1.5B_0\left[\left(\frac{V_0}{V}\right)^{7/3} - \left(\frac{V_0}{V}\right)^{5/3}\right]\left\{1 + 0.75(B_1 - 4)\left[\left(\frac{V_0}{V}\right)^{2/3} - 1\right]\right\} \quad (1)$$

where P is pressure, V_0 is the equilibrium volume, V is the deformed volume, B_0 is the bulk modulus, and B_1 is the derivative of the bulk modulus with respect to pressure. The bulk modulus of MoNbTaVW obtained by fitting the BM3-EOS to the P–V curve (red dash line in

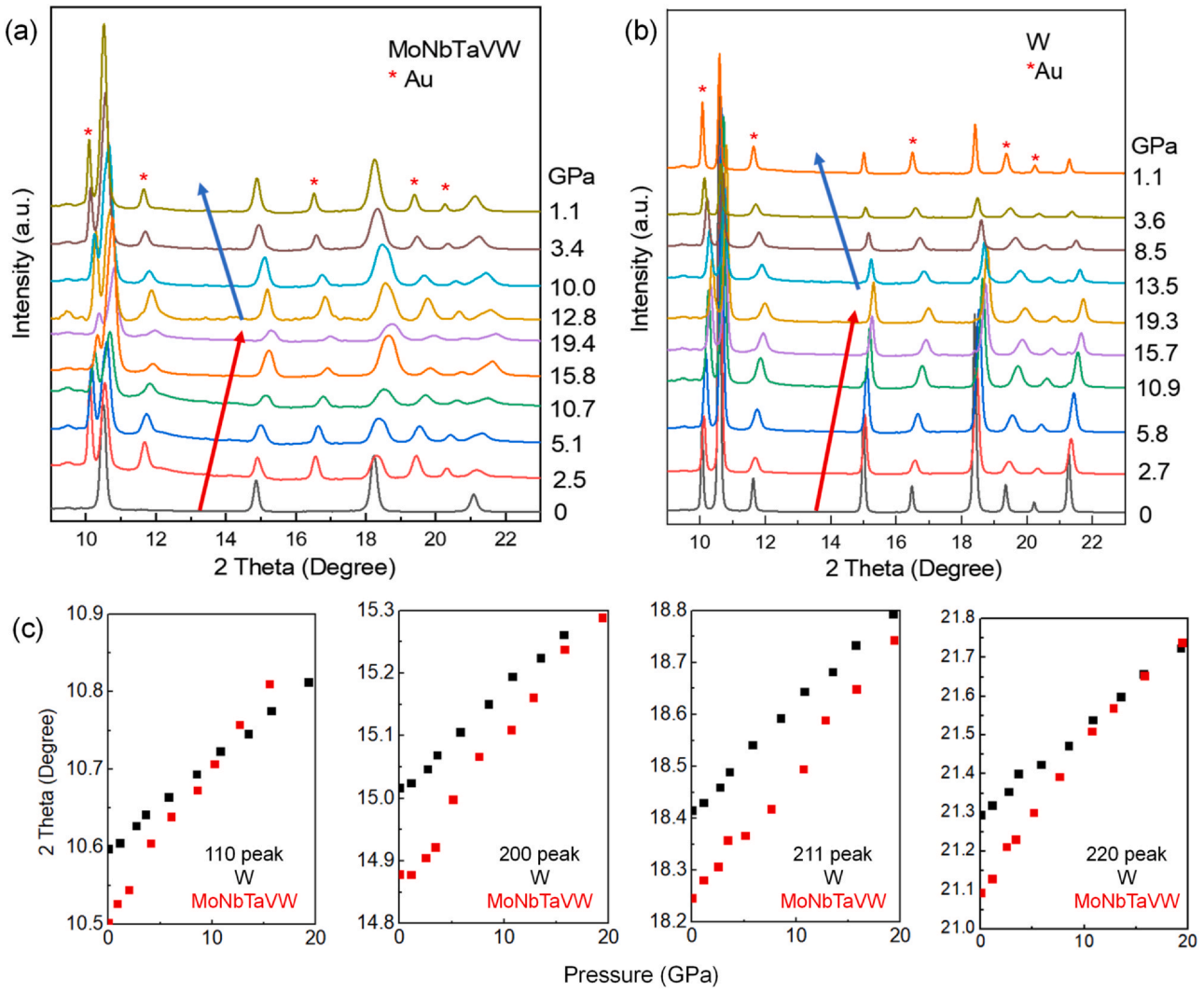

Fig. 2. (a) XRD patterns of the MoNbTaVW/Au mixture during compression and decompression; (b) XRD patterns of the pure W/Au mixture during compression and decompression. The corresponding pressures are marked on the right side of each XRD pattern. The red arrows in the figures indicate compression processes, while the blue arrows indicate the decompression processes. (c) 2 Theta as the function of pressure for 110, 200, 211 and 220 peaks.

Fig. 3(a)) is 201.7 ± 5.8 GPa, with a pressure derivative of 4 and an equilibrium volume of 16.307 Å^3/atom. The bulk modulus of W (black dash line in Fig. 3(a)) is 307.7 ± 4.1 GPa with a pressure derivative of 4 and an equilibrium volume of 15.810 Å^3/atom. The small bulk modulus of MoNbTaVW represents its higher compressibility, and consequently, the shift of the XRD peaks for MoNbTaVW is more obvious than those for W with the increase of pressure, as shown in Fig. 2.

The bulk moduli of MoNbTaVW and W were also estimated by fitting the data to the Voigt–Reuss–Hill averaging scheme [46] based on DFT,

$$B = \frac{1}{3}(C_{11} + 2C_{12}),\ G = \frac{1}{2}(G_{Voight} + G_{Reuss}) \quad (2)$$

$$G_{Voight} = \frac{1}{5}(C_{11} - C_{12} + 3C_{44}),\ G_{Reuss} = \frac{5}{4(S_{11} - S_{12}) + 3S_{44}} \quad (3)$$

where C_{11}, C_{12}, and C_{44} are the elastic constants, and S_{11}, S_{12}, and S_{44} are elements in the compliance matrix. The bulk moduli of MoNbTaVW and W obtained by the Voigt–Reuss–Hill scheme are 216.59 GPa and 324.53 GPa, respectively. The experimental lattice constants of MoNbTaVW and W that were measured under pressure, and those obtained from the DFT estimation based on the BM3-EOS, are shown in Fig. 3(b). As seen in the figure, the DFT simulations on the structural and mechanical properties are very close to the experimental observation. At 0 K, the simulated shear modulus (G), Young's modulus (E), and Poisson's ratio (ν) for MoNbTaVW are 57.62 GPa, 158.69 GPa, and 0.3750, respectively. The Vickers hardness, H_v, which was calculated by using Tian's model [47], is 3.72 GPa.

The azimuthally unrolled diffraction images as a function of direction angle for MoNbTaVW and W before compression, at ~5 GPa up to ~20 GPa, and after releasing pressure are shown in Fig. 4(a). The diffraction lines of Au are marked at the top of the figure. Curved diffraction lines under pressure indicate the existence of compressive stresses which lead to lattice strain. Under 20 GPa, curvature of the diffraction peaks for MoNbTaVW is much stronger than that of W, which represents larger lattice strain under high pressure. The alternative change of intensity on each diffraction line (peak) is induced by the development of dislocations under shear stress. Comparing with W, the texture of MoNbTaVW is much stronger, which suggests that the dislocation behavior is much more active in MoNbTaVW, and the dislocation density is consequently higher. Both MoNbTaVW and W form in the BCC structure with strong lattice strain and texture appearing at ~5 GPa. With the increase of pressure, no significant change in the diffraction lines was obtained in

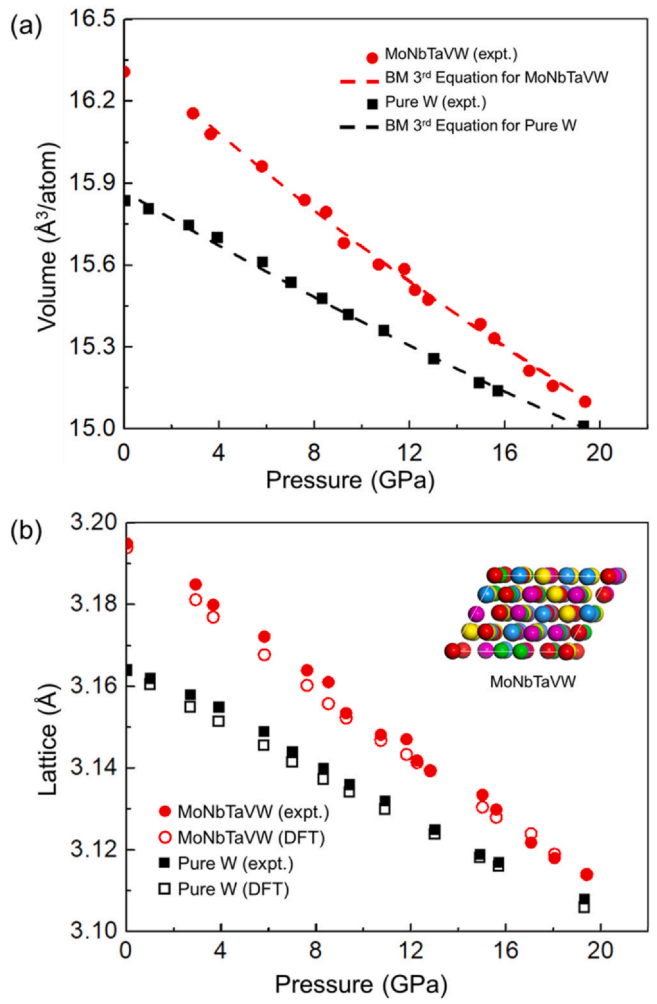

Fig. 3. (a) Volume as a function of pressure for MoNbTaVW (red circles) and W (black squares). (b) The lattice parameters of MoNbTaVW and W as a function of pressure. The dashed lines are fits to the BM3-EOS. The experimental lattice parameters are marked by solid squares/circles, and the DFT results are marked by hollow squares/circles. The 125-atom supercell of MoNbTaVW is shown in the inset.

the pressure range between 5 GPa and 20 GPa. After continually releasing pressure, no new diffraction lines appeared, indicating the phase stability of both MoNbTaVW and W. Similarly, the microstrain based on XRD line broadening in Fig. 2(a) as a function of pressure for both samples are shown in Fig. 4(b), where the black dots represent the microstrain of MoNbTaVW and red dots stand for the microstrain of W, respectively. The higher microstrain of MoNbTaVW indicates higher dislocation density since that microstrain is generally in proportional to the square root of dislocation density.

According to the lattice strain theory developed by Singh et al. [48–50], the stress state at the center of the specimen compressed nonhydrostatically in a DAC is given by,

$$\sigma = \begin{bmatrix} \sigma_1 & 0 & 0 \\ 0 & \sigma_1 & 0 \\ 0 & 0 & \sigma_3 \end{bmatrix} = \begin{bmatrix} \sigma_p & 0 & 0 \\ 0 & \sigma_p & 0 \\ 0 & 0 & \sigma_p \end{bmatrix} + \begin{bmatrix} -t/3 & 0 & 0 \\ 0 & -t/3 & 0 \\ 0 & 0 & 2t/3 \end{bmatrix} \quad (4)$$

where σ_3 and σ_1 are principle stresses along compression direction and radial direction, respectively, and σ_p is mean normal stress (equivalent hydrostatic pressure) in such a system. The difference between σ_3 and σ_1 is termed as differential stress t, $t = \sigma_3 - \sigma_1 = \leq 2\tau = \sigma_y$, where τ and σ_y is the shear strength and yield strength of the material, respectively.

The equation for the lattice strain and d spacing measured by X-ray diffraction in this system can be described as

$$d_m(hkl, \psi) = d_P(hkl)[1 + Q(hkl)(1 - 3\cos^2\psi)] \quad (5)$$

where $d_m(hkl, \psi)$ is the measured d-spacing, $d_p(hkl)$ is the hydrostatic d-spacing, ψ is the angle between the diffracting plane normal and the loading axis, and $Q(hkl)$ is the lattice strain parameter caused by deviatoric stress component, which is given by

$$Q(hkl) = (t/3)\{\alpha[2G_R(hkl)]^{-1} + (1 - \alpha)(2G_V)^{-1}\} \quad (6)$$

where $G_R(hkl)$ and G_V are the shear moduli of the aggregate under Reuss (isostress) and Voigt (isostrain) approximations, respectively. They are expressed as

$$[2G_R(hkl)]^{-1} = [S_{11} - S_{12} - 3(S_{11} - S_{12} - S_{44}/2)\Gamma(hkl)],$$

$$\Gamma(hkl) = (h^2k^2 + k^2l^2 + l^2h^2)/(h^2 + k^2 + l^2)^2, \quad (7)$$

and

$$(2G_V)^{-1} = 5S_{44}(S_{11} - S_{12})/[6(S_{11} - S_{12}) + 2S_{44}], \quad (8)$$

where S_{ij} are elastic compliances of material. Parameter α is a value between 0 and 1 describing the continuity behavior of the polycrystalline materials. If we assume isostress condition, the ratio of the differential stress to shear modulus would be $t(hkl)/G = 6 < Q(hkl) >$, which represents the lattice strain along the direction [hkl] of each observed reflection and can be used for a first evaluation of the stress level in plastically-deforming aggregates [51]. Fig. 5(a) shows $t(hkl)/G$ for MoNbTaVW and W. These values of MoNbTaVW are about three times larger than those of W, indicating a much higher stress level in the former sample. Our synchrotron XRD rDAC experiment, with an average particle size of ~1 μm, showed that both MoNbTaVW and W started to yield at a pressure of ~5 GPa. The t/G ratios for both samples increase from 0 to 5 GPa and then remain stable in the pressure range between 5 GPa and 20 GPa. This result indicates that the deformation remains elastic when the pressure is below 5 GPa, while plastic deformation begins above 5 GPa. In both samples, the ratio $t(200)/G$ has the smallest value, indicating that this is the softest plane and supports the lowest stress, while a larger lattice strain anisotropy is observed in MoNbTaVW. Fig. 5(b) compares the average differential stress (t) for MoNbTaVW and W based on the ratio t/G, where the shear moduli, G, under different pressures were obtained by the Voigt–Reuss–Hill averaging scheme based on DFT calculations. The differential stresses of both materials increase rapidly when the pressure is below 5 GPa and then increase slowly in the pressure range between 5 GPa to ~20 GPa. MoNbTaVW supports a differential stress of ~2.35 GPa when it starts to yield at ~5 GPa. It reaches 3.0 GPa when the pressure is about 19.4 GPa. Pure W displays a yield strength of ~1.5 GPa and it reaches 2.15 GPa at 19.3 GPa. Furthermore, the yield strength of MoNbTaVW is about 1.5 times higher than that of Xiong et al. [52] measured the stress of W with a particle size of 4–6 μm by non-hydrostatic compression using the same technique. The results showed that the stress of W reaches ~2 GPa when the pressure is 20 GPa [52], which is consistent with our observation. It is well known that atoms of different elements are distributed randomly in the crystal lattice of high entropy alloy, the different atomic properties and interactions make it hard for atoms to diffuse, which induce the high strengthening of the alloy. On the other hand, the elements contained in MoNbTaVW have high strength in their pure metal, which may enhance the property of alloy as well. Specifically, in this research, we further found that the texture of MoNbTaVW becomes stronger under high pressure, which indicates stronger dislocation interactions under stress. The details are described in next section.

Under uniaxial compression, differential stress impose both elastic and plastic strain in the specimen. The variations in peak positions with azimuthal angle represent elastic strain, while the

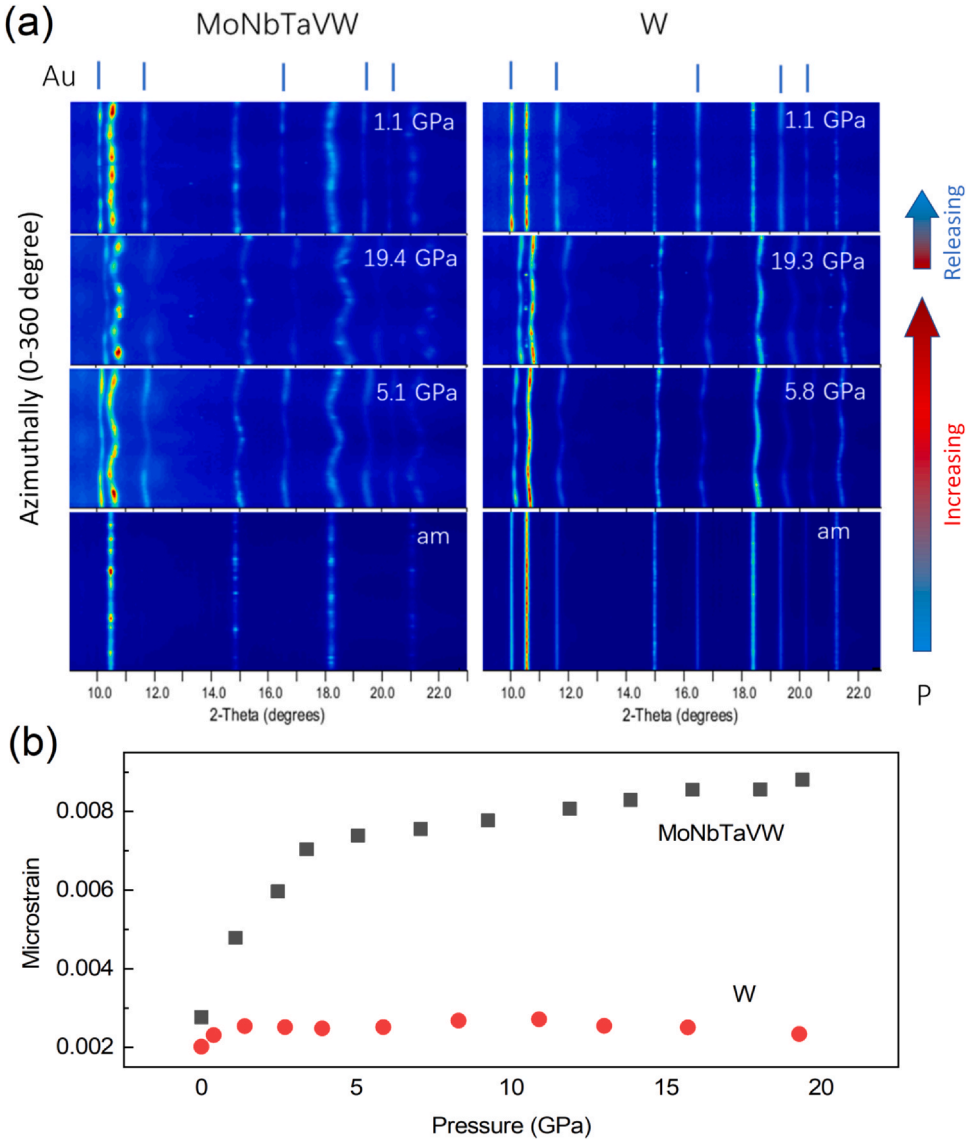

Fig. 4. (a) Azimuthally unrolled diffraction images under various pressures for MoNbTaVW (left) and pure W (right). The diffraction lines of Au are marked at the top of the figure. The pressures are marked on the right of each image. (b) Microstrain as the function of pressure for MoNbTaVW (black, square) and W (red, circle).

plastic strain induced lattice preferred orientation (LPO), or texture, is manifested by variations in peak intensity with azimuth in diffraction patterns. The lattice strain of the specimen was fitted with the "Radial Diffraction in the DAC" model in MAUD and $Q(hkl)$ could be directly obtained. Crystallographic textures were fitted using the E-WIMW algorithm, an extension of the WIMW algorithm [53], with an orientation distribution function (ODF) resolution of 15° and assuming cylindrical symmetry about the compression direction. The ODF was subsequently smoothed with 7.5° Gauss filter in Beartex to remove artifacts from the ODF resolution [54]. Finally, inverse pole figures (IPF) that show the relationship between crystallographic directions of crystallites to the compression direction were generated. For cubic crystal symmetry, a fundamental sector of the IPF between 001, 110, and 111 is sufficient to represent the whole ODF. Pole densities are given in multiples of a random distribution (m.r.d.), where mrd = 1 corresponds to a random distribution and an m.r.d. of infinity corresponds to a single-crystal texture.

IPFs of the compression direction were used to represent the texture. Fig. 6 shows the texture development of both the MoNbTaVW and pure W samples under pressure. Multiples of a random distribution (m.r.d.), which represent pole densities, under various pressure are marked by colors from blue (weak) to red (strong). At ambient conditions, both MoNbTaVW and W displayed a nearly random texture. With the increase of pressure, both samples developed a texture characterized by two maxima in the 100 and 111 directions and a minimum at 110. This is consistent with previous radial X-ray diffraction studies on W [52]. This texture also agrees with compression textures reported for BCC metals and is attributed to dominant slip on {110} < 111 > [55]. Very recently, F. Maresca's group [10] claimed that the edge dislocation plays an important role in the strengthening of BCC HEAs, based on both experimental and computational results, which are also consistent with the observations in this work. The maximum IPF of MoNbTaVW increased to 4.46 m.r.d. when the applied pressure was 19.4 GPa, while the maximum IPF of pure W increased to 1.56 m.r.d. at a pressure of 19.3 GPa. The stronger texture of MoNbTaVW under 20 GPa indicates higher dislocation activity, resulting in higher plastic deformation of the material [26,27]. Thus this is the first time *in situ* observation of the strength enhancement of MoNbTaVW under stress along with the nucleation of dislocations. The formation of a strong texture is an effective way to improve strength, the similar discovery has also been reported in Mg alloys [56] and Al alloys [57]. The IPF of both

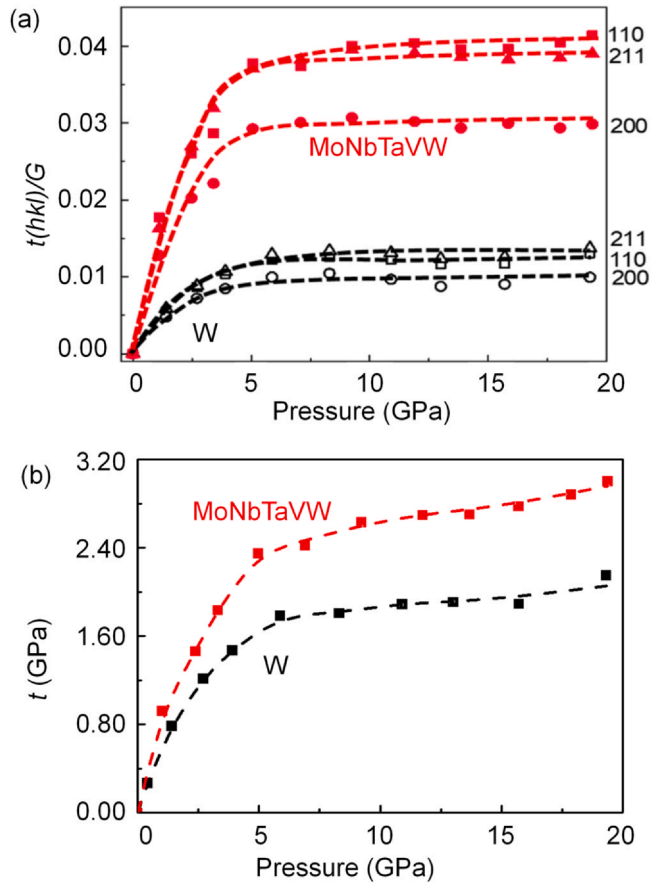

Fig. 5. (a) (Upper) Ratio of differential stress to shear modulus (t/G) as a function of pressure for MoNbTaVW (red) and pure W (black). (b) (Bottom) Differential stress (t) as a function of pressure for MoNbTaVW (red) and pure W (black).

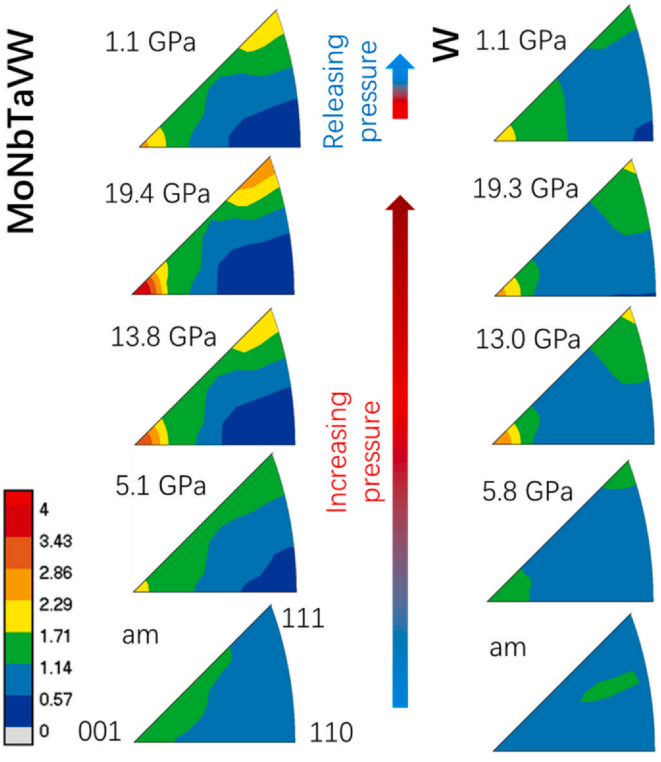

Fig. 6. Inverse pole figure (IPF) along the normal direction for MoNbTaVW (left) and pure W (right).

samples during decompression are shown at the top of Fig. 6. The texture of both samples has changed, as compared to that before compression. The maximum IPF of MoNbTaVW after releasing the pressure is 1.81 m.r.d., while that for pure W is 1.78 m.r.d., which indicates that part of the dislocation activity will recover when the pressure is released.

4. Conclusion

In this work, we have demonstrated a unique experimental method to study the deformation behavior of a high-entropy alloy MoNbTaVW under compression conditions *in situ*, by using synchrotron XRD and DAC techniques. Pure W metal was used as a reference sample. XRD patterns under various pressures illustrated that MoNbTaVW is more capable of resisting high pressure, and the strength of MoNbTaVW we obtained is about 1.5 times higher than that of pure W under compression. Due to the shear stress produced by DAC forces, both MoNbTaVW and W deform plastically under high pressure. The dislocation-induced texture in MoNbTaVW is much stronger than that of W. The origin of the high strength and phase stability in MoNbTaVW, and quite likely in all HEAs, resides in these strong active dislocations. This *in situ* method can also be used in other HEA dislocation slip systems, which will provide further understanding of the mechanism responsible for their excellent mechanical properties and help to design ultra-high-performance alloy materials required in various fields.

CRediT authorship contribution statement

Congyan Zhang: Conceptualization, Methodology, Data curation, Original draft preparation. **Binbin Yue:** Methodology, Data curation. **Uttam Bhandari**: Theoretical simulation. **Oleg N. Starovoytov**: Sample preparation. **Yan Yang**: Sample preparation. **David P. Young**: Resources. **Jinyuan Yan**: Resources. **Fang Hong**: Conceptualization, Original draft preparation. **Shizhong Yang**: Conceptualization, Supervision. All authors: Review and editing the manuscript.

Declaration of Competing Interest

The authors declare that they have no known competing financial interests or personal relationships that could have appeared to influence the work reported in this paper.

Acknowledgments

The Advanced Light Source is supported by the Director, Office of Science, Office of Basic Energy Sciences, of the U.S. Department of Energy [Grant No. DE-AC02-05CH11231]. We acknowledge partial support from NSF EPSCoR CIMM project [Grant No. 1541079], NSF (2019)-LINK-128, LAMDA project award No. 1946231 under SEED Track 1B support, DOE/NNSA [Grant No. DE-NA0003979], and Department of Defence support [Grant No. W911NF1910005]. D.P. Young acknowledges support from NSF [Grant No. DMR-1904636]. The computational simulations were supported by the Louisiana Optical Network Infrastructure (LONI) with the supercomputer allocation loni_mat_bio15. The work is also supported by National Natural Science Foundation of China [Grant No. 12004014, U1930401] and talent start-up funding from Institute of Physics, Chinese Academy of Sciences.

References

[1] P. Koželj, S. Vrtnik, A. Jelen, S. Jazbec, Z. Jagličić, S. Maiti, M. Feuerbacher, W. Steurer, J. Dolinšek, Discovery of a superconducting high-entropy alloy, Phys. Rev. Lett. 113 (10) (2014) 107001.
[2] H.-S. Do, B.-J. Lee, Origin of radiation resistance in multi-principal element alloys, Sci. Rep. 8 (1) (2018) 16015.

[3] D.B. Miracle, O.N. Senkov, A critical review of high entropy alloys and related concepts, Acta Mater. 122 (2017) 448–511.
[4] H.Y. Diao, R. Feng, K.A. Dahmen, P.K. Liaw, Fundamental deformation behavior in high-entropy alloys: an overview, Curr. Opin. Solid State Mater. Sci. 21 (5) (2017) 252–266.
[5] C. Lee, G. Song, M.C. Gao, R. Feng, P. Chen, J. Brechtl, Y. Chen, K. An, W. Guo, J.D. Poplawsky, S. Li, A.T. Samaei, W. Chen, A. Hu, H. Choo, P.K. Liaw, Lattice distortion in a strong and ductile refractory high-entropy alloy, Acta Mater. 160 (2018) 158–172.
[6] Y. Zhang, T.T. Zuo, Z. Tang, M.C. Gao, K.A. Dahmen, P.K. Liaw, Z.P. Lu, Microstructures and properties of high-entropy alloys, Prog. Mater. Sci. 61 (2014) 1–93.
[7] O.N. Senkov, G.B. Wilks, J.M. Scott, D.B. Miracle, Mechanical properties of $Nb_{25}Mo_{25}Ta_{25}W_{25}$ and $V_{20}Nb_{20}Mo_{20}Ta_{20}W_{20}$ refractory high entropy alloys, Intermetallics 19 (5) (2011) 698–706.
[8] S.W. Xin, M. Zhang, T.T. Yang, Y.Y. Zhao, B.R. Sun, T.D. Shen, Ultrahard bulk nanocrystalline VNbMoTaW high-entropy alloy, J. Alloy. Compd. 769 (2018) 597–604.
[9] O.N. Senkov, G.B. Wilks, D.B. Miracle, C.P. Chuang, P.K. Liaw, Refractory high-entropy alloys, Intermetallics 18 (9) (2010) 1758–1765.
[10] F. Maresca, W.A. Curtin, Mechanistic origin of high strength in refractory BCC high entropy alloys up to 1900K, Acta Mater. 182 (2020) 235–249.
[11] G.A. Salishchev, M.A. Tikhonovsky, D.G. Shaysultanov, N.D. Stepanov, A.V. Kuznetsov, I.V. Kolodiy, A.S. Tortika, O.N. Senkov, Effect of Mn and V on structure and mechanical properties of high-entropy alloys based on CoCrFeNi system, J. Alloy. Compd. 591 (2014) 11–21.
[12] A. Gali, E.P. George, Tensile properties of high- and medium-entropy alloys, Intermetallics 39 (2013) 74–78.
[13] K.B. Zhang, Z.Y. Fu, J.Y. Zhang, W.M. Wang, H. Wang, Y.C. Wang, Q.J. Zhang, J. Shi, Microstructure and mechanical properties of $CoCrFeNiTiAl_x$ high-entropy alloys, Mater. Sci. Eng. A 508 (1) (2009) 214–219.
[14] A.H. Chokshi, High temperature deformation in fine grained high entropy alloys, Mater. Chem. Phys. 210 (2018) 152–161.
[15] Q. Ding, Y. Zhang, X. Chen, X. Fu, D. Chen, S. Chen, L. Gu, F. Wei, H. Bei, Y. Gao, M. Wen, J. Li, Z. Zhang, T. Zhu, R.O. Ritchie, Q. Yu, Tuning element distribution, structure and properties by composition in high-entropy alloys, Nature 574 (2019) 223–227.
[16] S.W. Wu, G. Wang, J. Yi, Y.D. Jia, I. Hussain, Q.J. Zhai, P.K. Liaw, Strong grain-size effect on deformation twinning of an $Al_{0.1}CoCrFeNi$ high-entropy alloy, Mater. Res. Lett. 5 (4) (2017) 276–283.
[17] F. Otto, A. Dlouhý, C. Somsen, H. Bei, G. Eggeler, E.P. George, The influences of temperature and microstructure on the tensile properties of a CoCrFeMnNi high-entropy alloy, Acta Mater. 61 (15) (2013) 5743–5755.
[18] N. Kumar, Q. Ying, X. Nie, R.S. Mishra, Z. Tang, P.K. Liaw, R.E. Brennan, K.J. Doherty, K.C. Cho, High strain-rate compressive deformation behavior of the $Al_{0.1}CrFeCoNi$ high entropy alloy, Mater. Des. 86 (2015) 598–602.
[19] W.A. Bassett, Diamond anvil cell, 50th birthday, High Press. Res. 29 (2) (2009) 163–186.
[20] F. Zhang, Y. Wu, H. Lou, Z. Zeng, V.B. Prakapenka, E. Greenberg, Y. Ren, J. Yan, J.S. Okasinski, X. Liu, Y. Liu, Q. Zeng, Z. Lu, Polymorphism in a high-entropy alloy, Nat. Commun. 8 (1) (2017) 15687.
[21] P.F. Yu, L.J. Zhang, J.L. Ning, M.Z. Ma, X.Y. Zhang, Y.C. Li, P.K. Liaw, G. Li, R.P. Liu, Pressure-induced phase transitions in HoDyYGdTb high-entropy alloy, Mater. Lett. 196 (2017) 137–140.
[22] B. Cheng, F. Zhang, H. Lou, X. Chen, P.K. Liaw, J. Yan, Z. Zeng, Y. Ding, Q. Zeng, Pressure-induced phase transition in the AlCoCrFeNi high-entropy alloy, Scr. Mater. 161 (2019) 88–92.
[23] F. Zhang, H. Lou, B. Cheng, Z. Zeng, Q.S. Zeng, High-pressure induced phase transitions in high-entropy alloys: a review, Entropy 21 (2019) 239.
[24] G. Li, D. Xiao, P. Yu, L. Zhang, P.K. Liaw, Y. Li, R. Liu, Equation of state of an AlCoCrCuFeNi high-entropy alloy, JOM 67 (10) (2015) 2310–2313.
[25] P. Yu, L.J. Zhang, H. Cheng, H. Zhang, M.Z. Ma, Y. Li, G. Li, P. Liaw, R.P. Liu, The high-entropy alloys with high hardness and soft magnetic property prepared by mechanical alloying and high-pressure sintering, Intermetallics 70 (2016) 82–87.
[26] B. Chen, K. Lutker, S.V. Raju, J. Yan, W. Kanitpanyacharoen, J. Lei, S. Yang, H.-R. Wenk, H.-k Mao, Q. Williams, Texture of nanocrystalline nickel: probing the lower size limit of dislocation activity, Science 338 (2012) 1448–1451.
[27] B. Chen, K. Lutker, J. Lei, J. Yan, S. Yang, H.-K. Mao, Detecting grain rotation at the nanoscale, Proc. Natl. Acad. Sci. 111 (9) (2014) 3350–3353.
[28] B. Yue, F. Hong, N. Hirao, R. Vasin, H.-R. Wenk, B. Chen, H.-K. Mao, A simple variant selection in stress-driven martensitic transformation, Proc. Natl. Acad. Sci. 116 (30) (2019) 14905–14909.
[29] B. Yue, F. Hong, S. Merkel, D. Tan, J. Yan, B. Chen, H.-K. Mao, Deformation behavior across the zircon-scheelite phase transition, Phys. Rev. Lett. 117 (13) (2016) 135701.
[30] J. Lei, G. Akopov, M.T. Yeung, J. Yan, R.B. Kaner, S.H. Tolbert, Radial X-ray diffraction study of superhard early transition metal dodecaborides under high pressure, Adv. Funct. Mater. 29 (22) (2019) 1900293.
[31] M. Xie, R. Mohammadi, C.L. Turner, R.B. Kaner, A. Kavner, S.H. Tolbert, Lattice stress states of superhard tungsten tetraboride from radial x-ray diffraction under nonhydrostatic compression, Phys. Rev. B 90 (2014) 104104.
[32] C. Prescher, V.B. Prakapenka, DIOPTAS: a program for reduction of two-dimensional X-ray diffraction data and data exploration, High Press. Res. 35 (3) (2015) 223–230.
[33] H. Rietveld, A profile refinement method for nuclear and magnetic structures, J. Appl. Crystallogr. 2 (2) (1969) 65–71.
[34] L. Lutterotti, S. Matthies, H.-R. Wenk, A.S. Schultz, J.W. Richardson, Combined texture and structure analysis of deformed limestone from time-of-flight neutron diffraction spectra, J. Appl. Phys. 81 (1997) 594–600.
[35] P. Hohenberg, W. Kohn, Inhomogeneous electron gas, Phys. Rev. 136 (1964) B864–B871.
[36] W. Kohn, L.J. Sham, Self-consistent equations including exchange and correlation effects, Phys. Rev. 140 (1965) A1133–A1138.
[37] G. Kresse, J. Furthmuller, Efficient iterative schemes for ab initio total-energy calculations using a plane-wave basis set, Phys. Rev. B 54 (16) (1996) 11169–11186.
[38] J.P. Perdew, J.A. Chevary, S.H. Vosko, K.A. Jackson, M.R. Pederson, D.J. Singh, C. Fiolhais, Atoms, molecules, solids, and surfaces: applications of the generalized gradient approximation for exchange and correlation, Phys. Rev. B 46 (11) (1992) 6671–6687.
[39] J.P. Perdew, K. Burke, M. Ernzerhof, Generalized gradient approximation made simple, Phys. Rev. Lett. 77 (18) (1996) 3865–3868.
[40] H.J. Monkhorst, J.D. Pack, Special points for Brillouin-zone integrations, Phys. Rev. B 13 (12) (1976) 5188–5192.
[41] M.C. Gao, J.-W. Yeh, P.K. Liaw, Y. Zhang (Eds.), High-Entropy Alloys: Fundamentals and Applications, Springer International Publishing, Cham, 2016, pp. 333–368.
[42] H.W. Yao, J.W. Qiao, J.A. Hawk, H.F. Zhou, M.W. Chen, M.C. Gao, Mechanical properties of refractory high-entropy alloys: experiments and modeling, J. Alloy. Compd. 696 (2017) 1139–1150.
[43] X. Gonze, First-principles responses of solids to atomic displacements and homogeneous electric fields: implementation of a conjugate-gradient algorithm, Phys. Rev. B 55 (16) (1997) 10337–10354.
[44] F. Birch, Finite elastic strain of cubic crystals, Phys. Rev. 71 (11) (1947) 809–824.
[45] F.D. Murnaghan, The compressibility of media under extreme pressures, Proc. Natl. Acad. Sci. 30 (9) (1944) 244–247.
[46] L. Zuo, M. Humbert, C. Esling, Elastic properties of polycrystals in the Voigt-Reuss-Hill approximation, J. Appl. Crystallogr. 25 (6) (1992) 751–755.
[47] Y. Tian, B. Xu, Z. Zhao, Microscopic theory of hardness and design of novel superhard crystals, Int. J. Refract. Met. Hard Mater. 33 (2012) 93–106.
[48] A.K. Singh, C. Balasingh, H.K. Mao, R.J. Hemley, J. Shu, Analysis of lattice strains measured under nonhydrostatic pressure, J. Appl. Phys. 83 (12) (1998) 7567–7575.
[49] A.K. Singh, The lattice strains in a specimen (cubic system) compressed nonhydrostatically in an opposed anvil device, J. Appl. Phys. 73 (1993) 4278–4286.
[50] A.K. Singh, H.-k Mao, J. Shu, R.J. Hemley, Estimation of single-crystal elastic moduli from polycrystalline X-ray diffraction at high pressure: application to FeO and iron, Phys. Rev. Lett. 80 (1998) 2157–2160.
[51] P. Raterron, S. Merkel, C.W. Holyoke, Axial temperature gradient and stress measurements in the deformation-DIA cell using alumina pistons, Rev. Sci. Instrum. 84 (4) (2013) 043906.
[52] L. Xiong, B. Li, Y. Tang, Q. Li, J. Hao, L. Bai, X. Li, J. Liu, Radial X-ray diffraction study of the static strength and texture of tungsten to 96 GPa, Solid State Commun. 269 (2018) 83–89.
[53] S. Matthies, G.W. Vinel, On the reproduction of the orientation distribution function of texturized samples from reduced pole figures using the conception of a conditional ghost correction, Phys. Status Solidi (b) 112 (1982) K111–K114.
[54] H.-R. Wenk, S. Matthies, J. Donovan, D. Chateigner, BEARTEX: a Windows-based program system for quantitative texture analysis, J. Appl. Crystallogr. 31 (1998) 262–269.
[55] A.D. Rollett, S.I. Wright, Typical textures in metals, in: U.F. Kocks, C.N. Tomé, H.R. Wenk (Eds.), Texture and Anisotropy Preferred Orientations in Polycrystals and their Effect on Materials Properties, Cambridge University Press, Cambridge, 2000.
[56] F. Guo, H. Yu, C. Wu, Y. Xin, C. He, Q. Liu, The mechanism for the different effects of texture on yield strength and hardness of Mg alloys, Sci. Rep. 7 (2017) 8647.
[57] G. Nussbaum, P. Sainfort, G. Regazzoni, Strengthening mechanisms in the rapidly solidified AZ91 magnesium alloy, Scr. Mater. 23 (1989) 1079–1084.